Assessing drivers of high exhumation magnitudes and young cooling ages in the eastern central Andes, southern Peru (13–18°S)

Chloë O. Glover [a,*], Nadine McQuarrie [a], Sarah Falkowski [b], Todd A. Ehlers [b,1]

[a] *University of Pittsburgh, Department of Geology and Environmental Science, 4107 O'Hara Street, Pittsburgh, PA 15261, USA*
[b] *University of Tübingen, Department of Geosciences, Schnarrenbergstr. 94-96, 72076 Tübingen, Germany*

ARTICLE INFO

ABSTRACT

The potential structural controls on exhumation across the southern Peruvian Andes are not well understood, in part due to limited structural studies that co-locate with thermochronometric datasets. We integrate these two datasets and evaluate the relative contribution that fault geometry, magnitude, and shortening rate have on predicted cooling ages. Here we present a balanced cross-section constructed using new structural observations. This section, combined with existing thermochronometer data and a thermokinematic model, investigates the drivers of high exhumation and young canyon thermochronometric ages along the deeply incised Marcapata canyon in southern Peru. Together, these approaches constrain the timing and magnitude of exhumation in this portion of the southern Peruvian Andes and provide a mechanism for documenting how the internal architecture changes along strike.

The balanced cross-section (oriented N30E) covers the Subandean Zone to the northeast, the Marcapata canyon on the eastern flank of the southern Peruvian Andes, and the Altiplano-Eastern Cordillera boundary to the southwest (13–18° S). Exhumation is constrained by four low-temperature thermochronometer systems, including apatite and zircon (U-Th)/He (AHe and ZHe, respectively) and fission-track (AFT and ZFT, respectively). The youngest AHe (∼1–3 Ma), AFT (∼3–7 Ma), ZHe (∼4–7 Ma), and ZFT (∼14–17 Ma) ages are located in the center and valley bottom of the Marcapata canyon. The thermokinematically modeled cross-section produces cooling ages determined by fault geometry and kinematics. Reset ZFT ages require burial of Ordovician rocks in excess of 5.5 km above the original 6.5 km depositional depth. We find that the ZFT and ZHe ages in the Eastern Cordillera are sensitive to the history and magnitude of burial, age and location of uplift, and canyon incision. Canyon incision is required to reproduce the youngest canyon thermochronometric ages while slow shortening rates from ∼10 Ma to Present are required to reproduce interfluve thermochronometric ages. Shortening is accommodated by basement faults that feed slip up through three different décollement levels before reaching the surface. The proposed stacked basement geometry sets the first-order cooling signal seen in modeled ages. We determined that the total shortening in this section from the Subandean Zone to the Altiplano is 147.5 km, similar to shortening estimates in an adjacent thermo-kinematically modeled section in the San Gabán canyon 50 km to the southeast. Both the ZHe and ZFT ages in the Marcapata section (4–5 and 14 Ma) are noticeably younger than cooling ages from the San Gabán section (16 and 29 Ma). The Marcapata section's higher magnitude of exhumation is due to a repetition of basement thrusts that continues to elevate the Eastern Cordillera while active deformation occurs in the Subandean Zone. The youngest thermochronometric ages in all four systems are co-located with the overlapping basement thrust geometry. This basement geometry, kinematic sequence of deformation, and canyon incision co-conspire to produce the young cooling ages observed in the Eastern Cordillera.

1. Introduction

Interpreting the history of orogen topography and exhumation requires observations and models at the appropriate scale to differentiate between local (10's km), regional (100's km) and orogen-scale (1000 km) drivers of deformation. In the Central Andean Plateau, >20 years of research have documented the along-strike

* Corresponding author.
E-mail addresses: chloe.glover@pitt.edu (C.O. Glover), nmcq@pitt.edu (N. McQuarrie), sarah.falkowski@uni-tuebingen.de (S. Falkowski), todd.ehlers@glasgow.ac.uk (T.A. Ehlers).
[1] Now at: University of Glasgow, School of Geographical and Earth Sciences, Glasgow, UK.
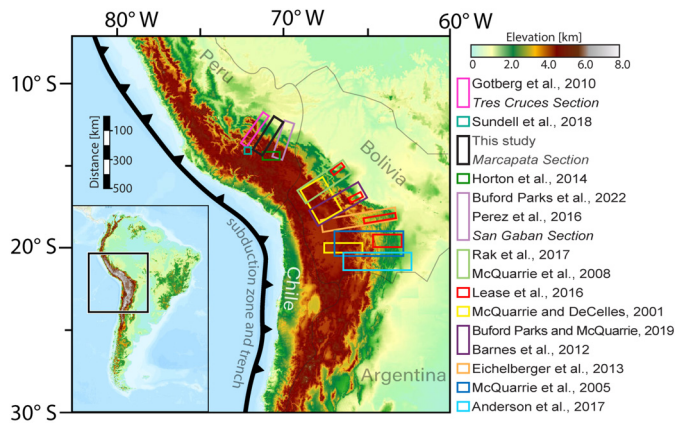
Fig. 1. Locations of geologic cross-sections across the eastern Central Andes in Bolivia and southern Peru.

The inset figure on the bottom left shows the map location of the main figure in South America. Colored rectangles correspond to the location of different studies listed on the right side of the figure. Light grey lines show simplified country boundaries. Thick black line with triangle teeth shows the location of the subduction zone. (Gotberg et al., 2010; Sundell et al., 2018; Horton et al., 2014; Buford Parks et al., 2023; Perez et al., 2016; Rak et al., 2017; McQuarrie et al., 2008; Lease et al., 2016; McQuarrie and DeCelles, 2001; Buford Parks and McQuarrie, 2019; Barnes et al., 2012; Eichelberger et al., 2013; McQuarrie et al., 2005; Anderson et al., 2017)

extent of features such as the first-order geometry of structures (Kley, 1996; McQuarrie, 2002; Müller et al., 2002; Elger et al., 2005; McQuarrie et al., 2008; Eichelberger et al., 2013; Anderson et al., 2017), exhumation (Benjamin et al., 1987; Barnes et al., 2006, 2008; Gillis et al., 2006; Eichelberger et al., 2013; Lease et al., 2016), the age and distribution of synorogenic sedimentary rocks (Horton et al., 2001; Horton, 2005; Garzione et al., 2014) and estimated rates of deformation (Oncken et al., 2006; Anderson et al., 2017; Rak et al., 2017; Buford Parks and McQuarrie, 2019) (Fig. 1). These Bolivian studies allow us to evaluate similarities and differences in the geometry, kinematics, and rate of deformation, relate deformation to surface uplift histories and assess changes in exhumation (e.g. Garzione et al., 2017). In the Peruvian Andes, where previous structural and exhumation studies are limited in extent and available data (e.g. Gotberg et al., 2010; Gautheron et al., 2013; Baby et al., 2018a,b; Gérard et al., 2021), or along single transects (Perez et al., 2016; Buford Parks et al., 2023), comparisons of geometry, kinematics, and their relationship to exhumation magnitude and age along strike are inhibited. The Marcapata canyon section presented in this study is an ideal location to assess along-strike continuity of structures and to decouple local vs orogenic drivers of exhumation because it is located between two previously published structural cross-sections and within a new regional thermochronometric dataset (Falkowski et al., 2023).

We present new structural mapping and accompanying geologic cross-section along the Marcapata canyon in southern Peru that provides a context for thermochronometer cooling ages (Falkowski et al., 2023). Together, the thermochronometric ages and their structural context allow us to quantitatively integrate structural geometry, uplift, erosion, and sedimentation across the Marcapata canyon (oriented N30E) and adjacent Eastern Cordillera to Altiplano region. Thermochronometer ages can be used to interpret the history of burial, uplift, erosion, deformation rate, and fault geometry proximal to sampled rocks. In this study, we evaluate the geometry and kinematics of our balanced cross-section and the resulting uplift and erosional exhumation history using apatite and zircon (U-Th)/He (AHe and ZHe) and fission-track (AFT and ZFT) low-temperature thermochronometers (Falkowski et al., 2023; Perez and Levine, 2020). Linking the flexural-kinematic bal-

anced cross-section to a thermokinematic model that predicts thermochronometric ages allows us to compare the basement geometry, fault geometry, uplift, and erosional exhumation history of our Marcapata section to the adjacent San Gabán section (Fig. 1; Perez et al., 2016; Buford Parks et al., 2023) and assess 1) whether the modeled geometry, kinematics, and rates are applicable over local to orogen scales, 2) the uniformity of internal architecture along-strike, and 3) the magnitude of canyon incision across southern Peru. Comparing along-strike cross-sections allows testing the sensitivity of exhumation to variations in structures, rates of shortening (Buford Parks et al., 2023) and Pliocene canyon incision (Lease and Ehlers, 2013; Falkowski et al., 2023), as well as gauging cross-section viability and along-strike extent of major structures; tasks imperative to understanding how internal architecture can manifest itself in differences of exhumation.

2. Background

2.1. Physiographic subdivisions

The Central Andes in southern Peru include four major physiographic subdivisions from east to west (Fig. 2C). The Subandean Zone (SAZ) is the most tectonically active physiographic province in the Central Andes with narrow east-verging Paleozoic thrust sheets and piggy-back basins (McQuarrie et al., 2008; Perez et al., 2016). The Eastern Cordillera (EC) is a northeastward-verging sequence of faults that expose the oldest and deepest rocks (dominantly Ordovician) and has peaks up to 6.4 km elevation. The boundary between the EC and SAZ is marked by a rapid increase in elevation from the modern foreland up to >3 km in the EC (Fig. 2A). The west-verging thrust faults of the western EC backthrust belt (McQuarrie and DeCelles, 2001; Perez et al., 2016) form the eastern side of a broad, low-relief, high-elevation plateau and the dominantly Tertiary basins of the Altiplano (AP) define the plateau center. The Western Cordillera (WC), marks the western plateau edge with topographic highs >6 km set by the active volcanic arc (Fig. 2).

2.2. Stratigraphy

The stratigraphy in the Peruvian Andes is comprised of ∼10 km of Ordovician through Tertiary sedimentary rocks (Fig. 2D). The Marcapata section can be divided into tiers based on distinct packages of rocks that deform similarly (Text S1). The lowest-level tier contains the Ordovician-aged San Jose and Sandia formations and ranges in thickness from ∼3.5 km in the AP to 4 km in the SAZ. The middle tier includes Silurian- through Triassic-aged units (Ananea, Cabanillas, Ambo, Tarma, Copacabana formations, and the Mitu Group; Fig. 2). The Permo-Triassic Mitu Group is not present in the SAZ and has a maximum exposed thickness of 1.3 km in the EC. The Silurian through Permian package ranges in thickness from 1.0 km in the AP to 1.1 km in the SAZ. The top tier of this system includes the Jurassic-aged Muni Formation through the Cretaceous Huancane Formation, Moho Group, Vilquechico Formation, and Paleocene-aged Auzangate Formation of the AP and EC with a combined thickness of 2.4 km. The SAZ Cretaceous package is 2.0 km thick and includes the Lower Cretaceous Oriente Formation, and the Upper Cretaceous Chonta and Vivian formations. Younger (<60 Ma) synorogenic sediments fill synclinal basins in the foreland and hinterland of the system. The AP consists of Tertiary sediment fill with a thickness of 7 km in the western AP basin (Descanso-Yauri Basin), and a thickness of 3 km in the easternmost AP basin (Sicuani Syncline) (Fig. 2).
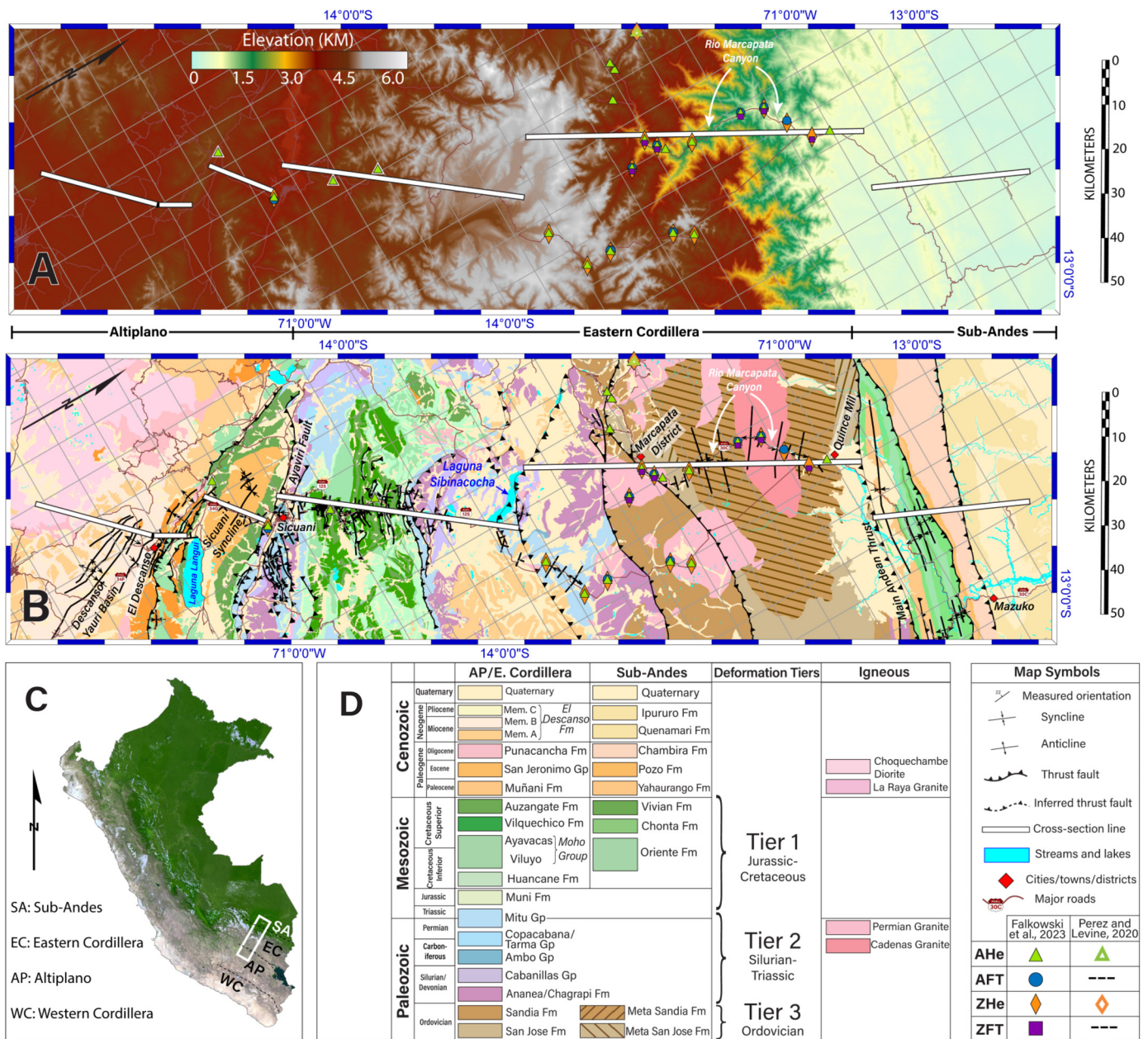
Fig. 2. Study area, geologic map, sample locations, and stratigraphy.
(A) Topographic map (based on a 30-m-resolution digital elevation model of Aster GDEM v2 and tandem-x data in WGS84 UTM (Zone 19S)) of the study area with cross-section lines shown in white (Lines 1–6 from southwest to northeast), and thermochronometer sample locations (Falkowski et al., 2023; Perez and Levine, 2020). (B) Geologic map of the study area with cross-section lines in white, and thermochronometer sample locations. See Fig. S1A for an enlarged version of the map and Fig. S1B for thermochronometer sample names and cross-section distances. (C) Study area (white rectangle) relative to Peru and four of the physiographic provinces (black dashed lines). (D) Stratigraphic column, map symbols, and key for panels A and B.

2.3. Previous thermochronology

In this study, we use a total of 49 AHe, AFT, ZHe, and ZFT ages (with 2σ-error) from 23 bedrock samples (Perez and Levine, 2020; Falkowski et al., 2023) within 35 km of our cross-section lines (Fig. 2A). The AHe, AFT, ZHe, and ZFT thermochronometer systems record cooling through approximately 68 °C (Farley, 2000), 110 °C (Ketcham et al., 2007), 180 °C (Reiners et al., 2004), and 240 °C (Brandon et al., 1998), respectively. Sampling through the EC to the SAZ boundary near Quince Mil was focused along the Rio Marcapata canyon that strikes perpendicular to mapped structures (Figs. 2A, 2B). Sample locations that were not immediately on our cross-section lines were projected along-strike, following major structural boundaries to the cross-section lines. Sample locations include high-elevation interfluves and canyon bottoms with over 1,600 m of relief in the EC (600–610 km in Fig. 3). The youngest cooling ages in the Marcapata section are from samples collected in the canyons (AHe ~1 Ma; AFT ~3 Ma; ZHe ~4 Ma; ZFT ~14 Ma), while interfluve ages are significantly older (AHe 4–20 Ma; AFT 10–16 Ma; ZHe >20 Ma).

2.4. Synorogenic basins

Synorogenic basins associated with fold-thrust belts form largely due to flexural loading from uplifted topography and record a linked deformation, erosional and depositional history (Horton et
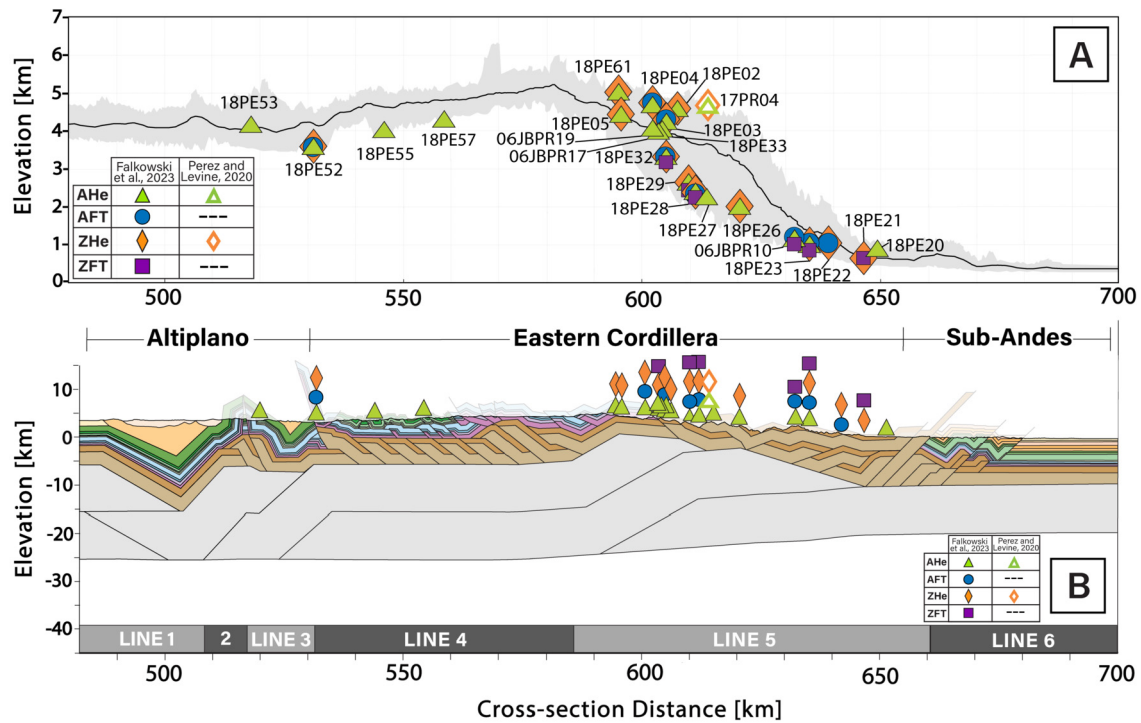
Fig. 3. Cross-section and location of thermochronometer samples.

(A) Thermochronometer sample elevations and locations along the topographic swath of the cross-section (Falkowski et al., 2023; Perez and Levine, 2020). Sample names are indicated. The black line shows the mean elevation, the grey shade shows the minimum and maximum elevation for a 50-km-wide swath encompassing the cross-section. The vertical exaggeration is x8. Eastern Cordilleran samples located at elevations higher/lower than the mean topography are defined as interfluve/canyon samples. (B) New balanced cross-section showing thermochronometer sample locations and distribution across different physiographic provinces. See Fig. 2D for cross-section stratigraphic unit key. The black lines that separate the Ordovician Sandia and San Jose formations represent fault lines. Areas without the black line separator indicate that the two Ordovician units were displaced as a cohesive unit. The lightest colored beds abode the modern topography lines represent eroded rocks. The four different symbols indicate the type of thermochronometer data available for each location (A, B). For readability, sample names are only shown in A. The extent of the different cross-section lines (1–6; cf. Fig. 2A, B) is indicated at the bottom.

al., 2014; Horton, 2018). The thicknesses of different sedimentary deposits, unit contacts, erosional contacts, unconformities, and the associated age data provide constraints for a modeled basin history (Text S1). The Paleogene San Jeronimo Group of the AP sits above the Late Cretaceous/Paleocene Auzangate Formation (Fig. 2B). In basins to the NW and SE, detrital zircon U-Pb data and measured strata provide basal age constraints of 41 Ma (Sundell et al., 2018) and 37 Ma (Horton et al., 2014), respectively, and thicknesses of ∼2.5–4 km for the San Jeronimo Group. The Oligocene-aged formations off-section to the NW and to the SE have measured thicknesses and ages of ∼1.4 km and 27–23 Ma (Sundell et al., 2018), and 1.1 km and 24–17 Ma (Horton et al., 2014; Perez and Horton, 2014), respectively. They either overlie the Paleogene San Jeronimo Formation in the NW (Horton et al., 2014; Sundell et al., 2018) or rest on an angular unconformity over older rocks in the SE (Perez and Horton, 2014). There is a record of growth strata from 28–25 Ma along the Ayaviri Fault that separates the AP from the EC (Horton et al., 2014) (Fig. 2B). The Miocene El Descanso Formation is composed of three members with a total thickness of ∼1.6 km in our section (Kar et al., 2016). Member A shows an angular unconformable relationship with the underlying San Jeronimo Formation. The contact between Member A and Member B was dated using biotite ^{40}Ar/^{39}Ar and is 19 Ma. The top of Member B is a low-angle unconformity and was dated with detrital zircon U-Pb at 9 Ma. Member C has a basal age of 5.4 Ma and a near-top contact age of 4 Ma based on detrital zircon U-Pb data (Kar et al., 2016). In contrast, a pronounced angular unconformity is observed in the NW basin between 23 and 10 Ma (Sundell et al., 2018).

3. Methods

3.1. Structural mapping

Mapping from 13 INGEMMET 1:100,000- and 1:50,000-scale geologic map quadrangles was used as coarse resolution base maps for the study area (Carlotto and Cárdenas, 2003; Cerrón and Chacaltana, 2003; Sánchez Izquierdo, 2003; Sánchez Fernández and Zapata Montes, 2003a; Sánchez and Zapata, 2003b; Quispesivana Quispe and Navarro Colque, 2003) and integrated with map data from previous studies (Horton et al., 2014; Saylor and Horton, 2014; Kar et al., 2016; Perez et al., 2016; Sundell et al., 2018). The integrated base maps were taken to the field in 2018 and revised with new observations of faults, folds, orientations, and lithologies. Observations and data were collected along canyons, interfluves, and major highways and compiled into a new geologic map (Fig. 2B, Fig. S1A) using ArcGIS.

3.2. Structural cross-section

Six section lines (Lines 1–6 from SW-NE) were chosen for cross-section construction based on proximity to mapped observations and orientations. Lines were oriented ∼N30E approximately perpendicular to the ∼NW/SE strike of major structures (Figs. 2B, 3). Regions without direct measurements and/or observations were interpolated based on regional map patterns and along-strike observations proximal to the transects.

The regional cross-section integrates the six section lines and reflects the new geologic map. The deformed and restored cross-sections were constructed concurrently by balancing each bed length in a section segment using sinuous and line-length balanc-

ing (Dahlstrom, 1969). Packages of rocks that deform similarly and share a common detachment horizon are referred to as tiers (Text S1; Figs. 2, 3). Each tier of strata was restored such that displacement from the basement had a kinematically viable path through each tier of the system to the surface, maintaining the same shortening magnitude.

Depth to the basement in the SAZ (9–10 km) and a ∼2° southwestward slope of the décollement are supported by 2D seismic sections from previous studies (Gil, 2002). Basement thrust sheets that fill space between Lower Ordovician rocks exposed at the surface and the southwestern continuation of the décollement are proposed to accommodate the structural relief (Fig. 2). We hypothesize that the region of high normalized channel steepness (K_{SN}) is located at and directly NE of the easternmost basement footwall ramp (610–615 km in Fig. S3, Text S2). A clear taper in both elevation and K_{SN} values from 615–650 km is used to identify the minimum width of previously uplifted topography and potential northeastern-most extent of the basement ramp hanging wall (Fig. 2; Fig. S3)(Eizenhöfer et al., 2019).

3.3. Flexural-kinematic modeling

The balanced cross-section was sequentially deformed in *Move.2019.1* with a 0.5×0.5 km grid of unique points to model the deformation, flexural loading, erosion, erosional unloading, sediment accumulation, and sediment loading in ∼10-km deformation steps (Table S2). Following deformation and loading, mean topography is simulated by assuming erosion occurs above a 2.5° topographic angle with maximum elevations at 6.5 km. For the final ∼7 km of model shortening, we apply a canyon topography with greater incision and an interfluve topography with lesser incision but use the mean topography to calculate flexure. Sedimentary basins created by flexural loading fill to 0 km elevation at each step (Text S3). Through the modeling process, we require that the cross-section model be balanced and have a viable kinematic deformation order. The flexural model must recreate the surface geology observations from the geologic map with the appropriate lithologies, orientations, basin depths, and elevations (e.g. McQuarrie and Ehlers, 2015; Rak et al., 2017; Buford Parks and McQuarrie, 2019; Braza and McQuarrie, 2022; Buford Parks et al., 2023).

3.4. Thermokinematic modeling

We applied a modified version of the *Pecube* thermokinematic model (Braun, 2003) called *Pecube-D* (Text S4) (Whipp et al., 2009; McQuarrie and Ehlers, 2015; Ehlers, 2023). The boundary conditions, thermophysical parameters and other model parameters used are provided in Table S3. An initial, steady-state solution was calculated using these parameters 50 Myr prior to the start of deformation. The kinematic field in *Pecube-D* was determined from displaced points in the kinematic model. The age of each 10-km deformation step was a free parameter and determined the velocity field and shortening rate (Table S5). Following this, the subsurface evolution of temperatures was calculated and thermochronometer ages were predicted for different thermochronometer systems at each step using prescribed kinetics (e.g., Ehlers, 2005)(Text S4). The predicted ages were compared to observed ages following the approach of previous work (e.g. McQuarrie and Ehlers, 2015; Ghoshal et al., 2020)(Text S4). The source code and a singularity container for the version of *Pecube-D* used in this study is freely available in Ehlers (2023).

We tested a suite of different thermokinematic models that evaluated the (1) sensitivity to assigned velocity, (2) age of canyon incision, (3) surface radiogenic heat production (A_O) and (4) out-of-sequence (OOS) faults. Model start time is constrained by the oldest measured reset ZFT and ZHe ages in the EC that range from 27 ± 5 to 56 ± 9 Ma (Falkowski et al., 2023; Perez and Levine, 2020). Velocity variations (1) included constant velocity (45 Ma start) and variable velocity (50 Ma start) model consistent with the best-fit velocity from Buford Parks et al. (2023). This applied velocity is 3.5 km/Myr until the last 10 Myr of the model, where the rates decrease to 0.6 km/Myr, and then 1.0 km/Myr for the final 3 Myr.

The effect of canyon incision (2) on modeled thermochronometric ages is evaluated by modeling both canyon and interfluve topography from 10 Ma or 3 Ma to Present. Canyon topography follows the shape of the modern topographic river bottom in the EC and reaches 0 km in the SAZ to match the basin fill level in the model. The interfluve topography follows the highest elevations over the same physiographic provinces (Fig. 3A). We tested a range of radiogenic heat production values (3) discussed further in the Supplementary Materials (Text S4; Table S3; Fig. S5). Time-temperature paths were produced using the *Pecube-D* thermal model outputs at selected points that correspond to thermochronometer sample locations using values between 3.0–4.0 μW/m^3 (Fig. S5). Finally, we tested an additional OOS fault (4) with 2 km of displacement to evaluate if local increases in exhumation are required to reproduce young, canyon ZHe ages (Section 5.3) (Fig. S6).

4. Results

4.1. Map patterns and resulting cross-section

Map patterns in the SAZ indicate two dominantly NE-verging faults. The frontal fault places Oligocene-aged rocks over the modern Quaternary foreland basin. The second fault to the SW carries folded Cretaceous rocks in the hanging wall and places them over Paleocene strata. The folds have wavelengths of 1–2 km (Fig. S1; Text S1). We show that the structural elevation of the folded Paleocene–Cretaceous rocks is the result of structurally repeated Ordovician rocks at depth (Fig. 3). The east-verging Main Andean Thrust separates the SAZ from the EC and places fine-grained micaceous quartzites and slates on Cretaceous rocks.

We identified metamorphosed Ordovician San Jose Formation in the immediate hanging wall of the Main Andean Thrust consistent with published map data, structural observations, and cross-section interpretations ∼50 km to the southeast (San Gabán) and northwest of our section (Perez et al., 2016; Gotberg et al., 2010). The Ordovician strata are folded with local exposures of Silurian rocks preserved in the cores of synclines across a map distance of 40–50 km and interpreted to be a roof thrust over duplexed Ordovician (and potentially younger) rocks (Gotberg et al., 2010; Perez et al., 2016; Text S1).

Southwest of the roof thrust are a series of southwest-verging and east-dipping thrust faults that place Ordovician rocks on Silurian rocks. The Silurian through Triassic section is repeated for 42 km of the cross-section (Lines 5 and 4) until a west-verging fault places the Permo-Triassic Mitu Group over Cretaceous sedimentary rocks (Fig. 2; Fig. 3). The backthrust belt of Cretaceous rocks displays 1–2 km wavelength fault-propagation folds exclusively repeating a package of Jurassic through Upper Cretaceous rocks along 25 km of the section (Fig. 2, 3). The westernmost EC fault (the Ayaviri Fault) places Silurian over Cretaceous rocks as the map transitions into predominantly Tertiary AP sedimentary rocks. The documented shortening in the Cretaceous in the backthrust belt is balanced by shortening in the Silurian–Triassic and by an Ordovician duplex at depth (Fig. 2, 3).

In the AP, the Sicuani Syncline (∼14 km wide along section) contains Cretaceous through Paleogene sedimentary rocks. The boundary between the Sicuani Syncline and the Descanso-Yauri Basin (∼20 km wide along section) places Early Cretaceous

rocks from the Sicuani Syncline on top of steep to overturned Paleogene conglomerates and sandstones of the Descanso-Yauri Basin. This boundary is mapped as a west-verging fault structure (Fig. 2). At depth, we infer a duplex of Ordovician rocks feeding slip to the younger Silurian through Cretaceous rocks at the surface, ultimately placing Early Cretaceous rocks on Paleogene rocks.

The Lower Ordovician rocks exposed at 3–4 km elevation in the EC combined with the depth of Ordovician rocks under the foreland basin and the Descanso-Yauri Basin (Fig. 3) requires basement deformation to explain these changes in structural elevation. In addition, the shortening accommodated by the repetition of basement thrusts has to equal and be kinematically viable with shortening amounts documented by surface structures (McQuarrie, 2002; McQuarrie et al., 2008). We place the easternmost basement thrust near the transition from EC to SAZ. The amount of shortening on this basement thrust must equal SAZ shortening and is currently active. Active uplift at the basement ramp produces high K_{SN} values (Fig. S3). The drop in elevation and K_{SN} values to background levels denotes the edge of the previously uplifted topography, formed and translated by the active basement thrust (Fig. 3; Fig. S3; Text S2) (Eizenhöfer et al., 2019). This relationship argues for 35 km of shortening of the eastern basement thrust sheet and the SAZ to the NE. Exposure of Ordovician rocks at 4 km in elevation requires stacking two basement thrusts above the active ramp at ∼600 km (Fig. 3). The footwall cut off of this second basement thrust is interpreted to set the EC/AP boundary at 540 km. Similarly, structural highs within the AP are proposed to result from displacement on basement thrusts (Fig. 3).

4.2. Sequential deformation, thermochronometric ages, and basin formation

The relationship between sequential deformation, basin formation, and thermochronometric age throughout the Marcapata section is synthesized in the sequential thermokinematic model results shown in Fig. 4 and examined in the following text. The following sequence is the result of iterative processes (Text S3, S4) that refined cross-section geometry, kinematics, and timing of deformation to best match measured data.

4.2.1. Initial EC deformation and backthrust belt

Model shortening initiated first in the basement that subsequently becomes the AP/EC boundary and then moves east to the primary basement fault under the EC. The faults fed slip to the east via Ordovician and younger rocks, and to the west via Silurian and younger rocks. Associated exhumation produces reset AHe ages and partially reset AFT ages in the east (∼580 km), and partially reset AHe ages in the west (∼500 km, Fig. 4B). From ∼48–33 Ma, eastward displacement on the basement thrust under the EC is accommodated by west-vergent shortening in Ordovician through Cretaceous rocks and the development of an east-verging roof thrust over the Ordovician San Jose and Sandia formations. Shortening in Silurian and younger rocks is focused above the roof thrust to facilitate burial (580–600 km, Fig. 4C). Loading from the basement thrust and the associated deformation in Ordovician and younger rocks creates four sedimentary basins, the future Altiplano Basin in the far west, two piggy-back basins that bury rocks in the EC, and the nascent foreland basin in the SAZ. The model predicted cooling signal above the basement ramp in the growing EC (490–530 km, Fig. 4C) displays fully reset AHe, AFT, and ZHe ages. Exhumation above thrust-repeated Silurian through Cretaceous rocks in the east produces reset AHe ages and partially reset AFT ages.

4.2.2. Continued EC deformation

Between 33 and 18 Ma, continued motion on the EC basement thrust is balanced by west-verging shortening in the backthrust belt and east-vergent propagation and growth of the roof thrust and associated faulting in Silurian–Tertiary rocks in the EC. This shortening and associated exhumation are reflected in the wide zone of modeled reset AHe and AFT ages from 490–620 km (Fig. 4D, E), and reset ZHe ages over the EC basement thrust and eastern duplex (590–620 km). Exhumation accompanying westward younging displacement in the backthrust belt is seen in the increasingly younger reset AHe and AFT ages to the west.

4.2.3. Altiplano

Shortening of the basement at the AP-WC boundary from 27–15 Ma drives surface shortening and enhances the partition between the Descanso-Yauri and Sicuani basins (Fig. 4D). Displacement on this basement fault is transferred to the surface via a west-verging fault repeating Ordovician through Cretaceous rocks. The modeled Paleogene (∼40–23 Ma) strata in the Descanso-Yauri Basin are 2.7 km thick, comparable to the measured thickness of the Paleogene San Jeronimo Group (∼2.8 km) 70 km northwest of our section (Sundell et al., 2018). The modeled Sicuani Basin accumulated 1.9 km of sediment during the same period. The Ayaviri Fault was active between 24–20 Ma in the model, creating an unconformity. This fault movement is younger than the ∼27 Ma growth strata along the Ayaviri Fault ∼50 km to the SE (Horton et al., 2014) but of similar age to the 18–23 Ma AHe ages along the fault (Perez, 2015).

4.2.4. SAZ and El Descanso-Yauri basin in the AP

After ∼18 Ma, shortening is focused in the eastern SAZ via motion on the easternmost basement thrust sheet. Uplift and associated exhumation over the active ramp produces young reset AHe, AFT, and ZHe model ages and 12 Ma reset ZFT model ages (Figs. 4F, G). These ages are the youngest over the active ramp (∼600 km) and increase in age to ∼18 Ma at 640 km. The Main Andean Thrust formed as an OOS fault placing Ordovician over Cretaceous rocks and separating the EC from the SAZ. Model predicted AHe, AFT, and ZHe ages are all reset, and ZFT ages partially reset at this OOS fault location near 660 km. The final deformation steps deform the Cretaceous through Tertiary rocks in the SAZ (Fig. 4H).

During SAZ deformation, our model accumulates 1.3 km of sediments in the Altiplano Descanso-Yauri Basin between ∼24 and 3 Ma and 0.4 km of Quaternary fill, comparable to measured data (Kar et al., 2016).

4.3. Fit to measured data

The model predicted ages are shown with a ±2 Myr uncertainty that represents the mean 1σ error of all the samples and ∼10% of the mean sample age. We use a 2.5 km lateral error to account for sample projection to the cross-section lines. The predicted ages are considered to match the measured ages when they intersect the sample's 2σ error bar(s). Samples to the east of the drainage divide are classified as either canyon or interfluve samples based on their location and relative elevation and are plotted separately in Fig. 5. We discuss the fit of the model to the measured data by highlighting the number of samples that are matched within error, as well as the across-strike pattern of measured and modeled ages.

To the west of the drainage divide, AP modeling results match three of four AHe samples and the single ZHe and AFT samples. The modeled AHe ages are ∼5 Myr older than the mean measured ages, though the shape of the resulting cooling path mimics that seen in the measured data (Fig. 5). East of the drainage divide, our model matches 76% of the interfluve samples: seven of
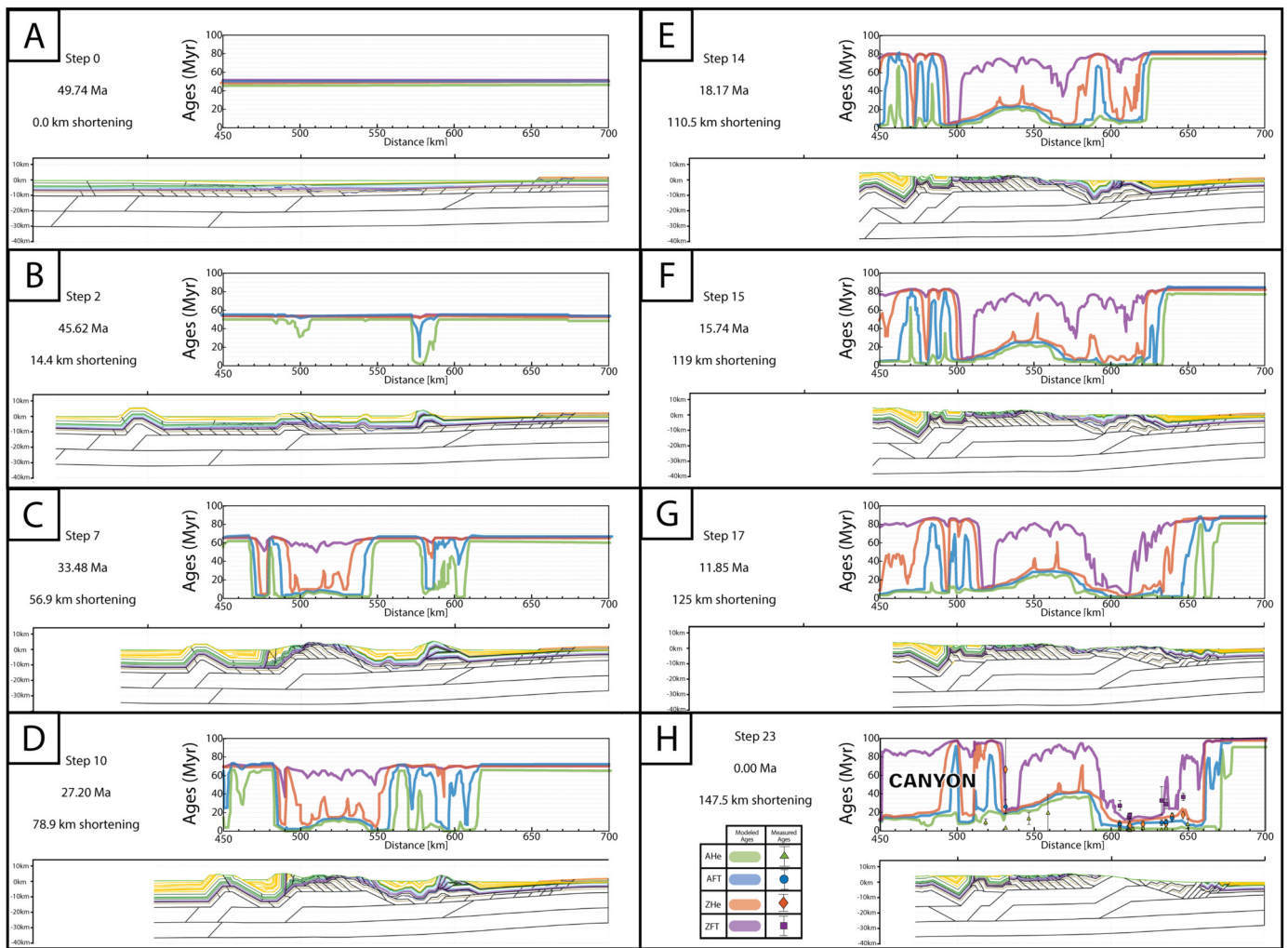
Fig. 4. Best model. Eight selected time steps in the variable velocity thermokinematic model (shortening rates of 3.5 km/Myr at 50–10 Ma, 0.6 km/Myr at 9–3 Ma, and 1.0 km/Myr at 3–0 Ma; cf. Table S4).

Each panel, A–H, shows the step number, associated time, and kilometers of shortening on the left. The top section of each panel shows the modeled ages for each thermochronometer, AHe (green), AFT (blue), ZHe (orange), and ZFT (purple). The kinematic model is on the bottom of each panel for the corresponding step. Colors in the kinematic model indicate unit ages: Cambrian–Precambrian basement (black), Ordovician (brown), Silurian–Permian (purple-blue), Triassic–Cretaceous (green), and Cenozoic (yellow). The cooling ages in panel A are all at 50 Myr because the thermal model is permitted 50 Myr to equilibrate crustal temperatures prior to initiation of deformation (model time shown in panel A) (Text S3). Areas where modeled ages are younger than adjacent ages (e.g. 570–580 km in panel B) correspond to exhumation driven by shortening and erosion (evident in the bottom section of each panel at the same distance along section) that have reset the modeled ages. See Fig. 2D for a more detailed stratigraphy. Panel H shows, in addition, the measured canyon thermochronometer samples from Falkowski et al. (2023).

nine AHe samples, both AFT samples and four of six ZHe samples. However, the model predicts interfluve ZHe ages that either overlap only at the youngest limit of 2σ error of the measured ages or are younger by 5–15 Myr between 600 and 610 km (Fig. 5A; Table S6). The model also produces AHe ages ∼5 Myr younger than two measured AHe ages. Thermal model results match all canyon samples from the AHe, AFT, and ZFT thermochronometers, and four of seven ZHe samples. The modeled ages are <4 Myr older than the three measured ZHe ages that are not matched (Fig. 5B).

4.4. Predicted time temperature paths

We compare the thermal history from inverse modeling of thermochronometer data from Falkowski et al. (2023) using *QTQt* (Gallagher, 2012) to time-temperature (tT) paths predicted from our *Pecube-D* simulation in Fig. 6. This comparison was conducted to assess misfits of modeled rock cooling due to sample erosional or deformation histories not evident from the patterns of predicted ages (Fig. 5) and to identify similarities and differences between

QTQt and *Pecube-D* tT paths. The temperature ranges for each sample, shown in grey in Fig. 6, were obtained using a range of surface heat production values (3.0–4.0 μW/m^3). We find that the tT-paths from *Pecube-D* modeling for SAZ samples (18PE22, 18PE20), and an EC interfluve sample (18PE05) overlap the *QTQt* tT-paths presented by Falkowski et al. (2023) (Fig. 6) and reproduce the measured ages for each. Interfluve sample 18PE04 has a *Pecube-D* tT-path that is similar in shape to the predicted *QTQt* path but is shifted ∼5 Myr older and up to 100 °C hotter. The AHe measured age is ∼5 Myr older than the modeled *Pecube-D* age (Fig. 5).

Pecube-D tT-paths for EC canyon samples 18PE28, 18PE23, and 16JBPR10 overlap with portions of the *QTQt* tT-paths, particularly at the higher and lower temperature ranges (Fig. 6H–K). These samples reproduce the measured ages for AHe, AFT, and ZFT, but *Pecube-D* results predict ZHe ages that cool ∼5 Myr earlier than shown in the *QTQt* cooling paths. The largest difference is observed in the tT-path from AP sample 18PE52 where no part of the predicted *Pecube-D* path matches the *QTQt* tT-path (Fig. 6B). The *Pecube-D* models suggest a 175 °C difference in temperatures at 30 Ma due to sedimentary burial that the sample may not have
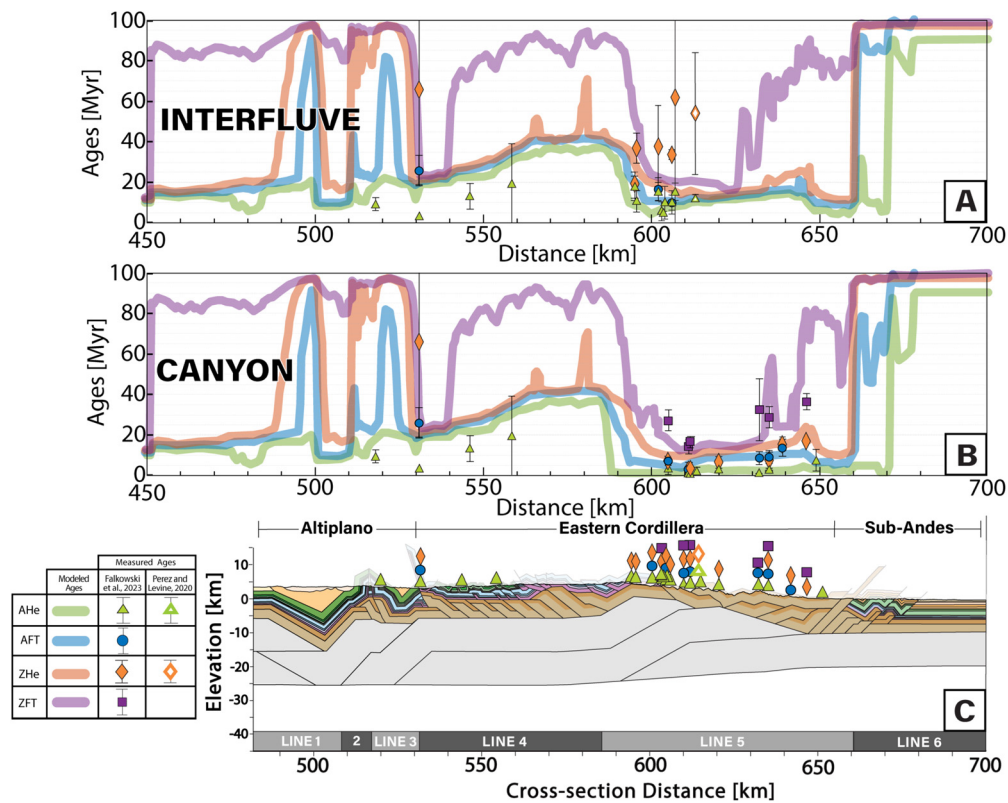
Fig. 5. Interfluve and canyon thermal modeling results.
Modeled (colored lines) and measured (data symbols with 2σ error bars) interfluve (A) and canyon (B) ages over the cross-section (C). Lateral distance error bars are not shown.

experienced (Figs. 6B, 4C). These differences in cooling histories are discussed in Section 5.3.

5. Discussion

5.1. Map pattern and associated structures

Previous studies have proposed that basement thrust faults are required to both accommodate the structural relief in the Peruvian Andes and minimize shortening estimates (Gotberg et al., 2010; Perez et al., 2016). Ordovician rocks currently exposed at >4 km elevation for ∼250 km along-strike in the Peruvian EC today were at an estimated depth of 10 km at approximately 45–50 Ma according to projections guided by mapped thicknesses (Fig. 2) and seismic studies that constrain the décollement depth and angle (Gil, 2002). We propose a two-tier basement ramp system that accommodates the same displacement as recorded in the Paleozoic and younger stratigraphic section and fills the space between the modern topography and the basement décollement. Accounting for change in structural elevation without basement involvement doubles the total estimated shortening (e.g., McQuarrie, 2002; Gotberg et al., 2010). A single basement ramp (Gotberg et al., 2010) requires an active ramp and uplift within the AP. In contrast, the two-tiered basement geometry presented here 1) co-locates the ramp with active uplift, high elevations, and high K_{SN} values in the EC, and 2) sets the first-order pattern of predicted cooling ages that match measured ages (Figs. 4, 5, 6).

The distinct packages of rocks that deform similarly across this portion of Peru are interpreted to have décollements in weak layers that partition the stratigraphy into three tiers based on packages of stratigraphy that are structurally repeated in the field (Fig. 2). These weak décollements have been shown to limit internal strain (Eichelberger and McQuarrie, 2015). Previous studies

depict the Silurian/Devonian through Cretaceous rocks deforming as a cohesive unit (Gotberg et al., 2010; Perez et al., 2016) except for a section of folded and faulted Cretaceous rocks immediately SW of the San Gabán section Macusani Structural Zone (Perez et al., 2016). In contrast to these sections, the Silurian through Permian section and Jurassic and younger rocks are always separated by mapped thrust faults in our study area (Fig. 2). The thickness and extent of weak mudstones in the Jurassic Muni Formation (Sempere et al., 2002) facilitates this upper décollement horizon and the narrow wavelength folds in Cretaceous rocks (Fig. 2; Text S1).

Previous shortening estimates for the neighboring San Gabán section, ∼50 km to the ESE, was 130 km (Perez et al., 2016). Extending this section to the southwest to include AP shortening increases the shortening amount to 150.7 km (Buford Parks et al., 2023), consistent with our estimated 147.5 km of shortening through the SAZ to the AP.

5.2. Required burial to reset ZFT

Fault displacement and deformation alone do not provide enough burial and subsequent exhumation to reproduce the measured 14–37 Ma ZFT ages (Fig. S4). Reset ZFT ages reveal areas where burial through thrust loading is needed to explain cooling from levels deeper than suggested by the regional stratigraphy alone. Thus, the modeled ZFT ages provide additional constraints for the burial and exhumation history. In particular, the Ordovician roof thrust needs 11–12 km of burial when the thrust is active (Fig. 4B–D) to reach ZFT closure temperatures. Without burial, these rocks will never reach temperatures needed to reset or partially reset the ZFT system (Buford Parks et al., 2023) (Fig. S4).

Reproducing the reset ZFT ages in the EC requires burial of the western end of the roof thrust that carries Ordovician age rocks
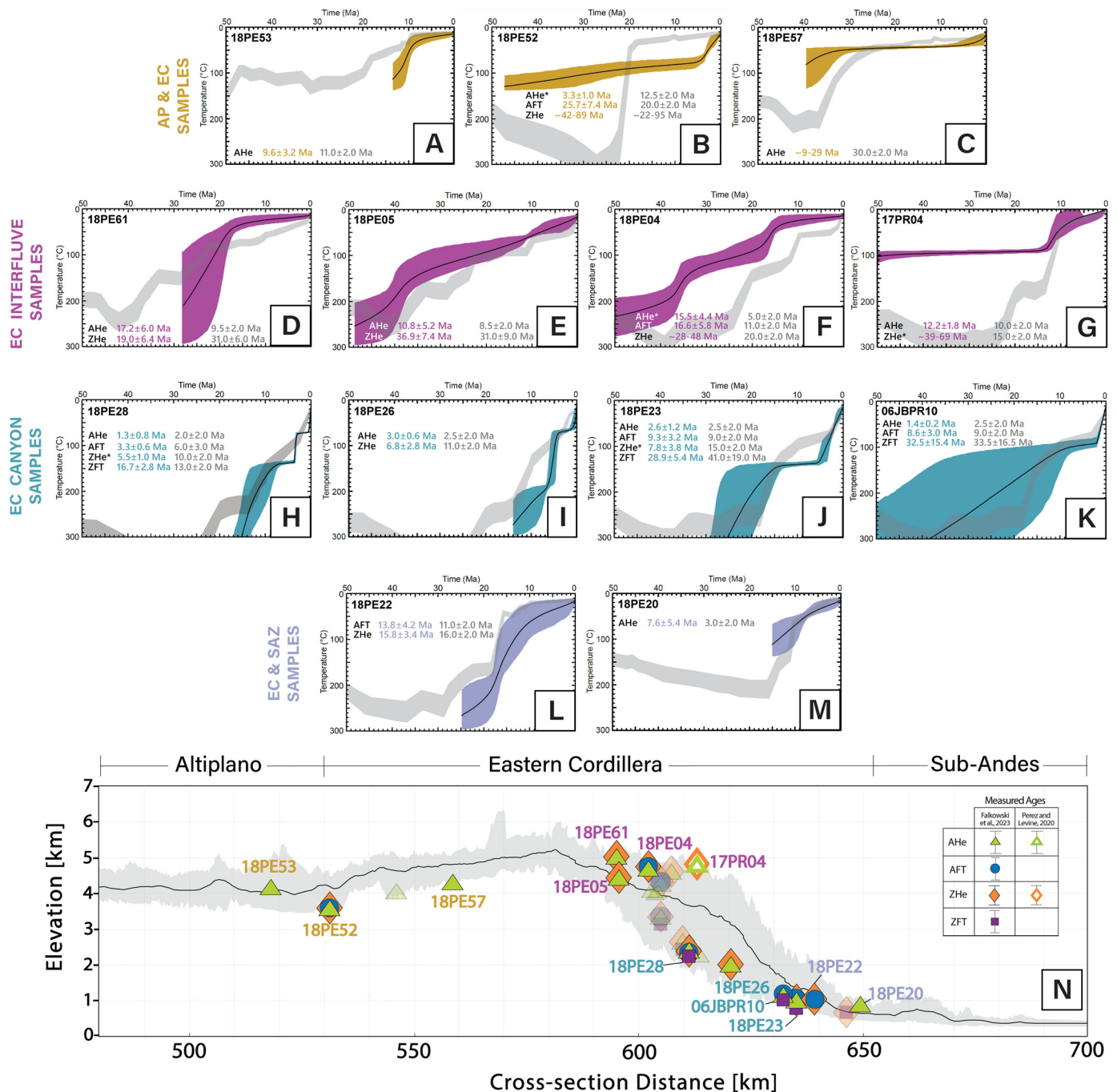
Fig. 6. Time-Temperature Histories.
tT histories of 12 selected samples (A–M), identified on the elevation-distance plot (N) over swath topography (defined in Fig. 3A). Elevation and location for the remaining samples are shown in panel N as unlabeled transparent symbols. Selected samples (A–M) best represent the tT histories in modeled *QTQt* cooling paths (colored bands) as determined by Falkowski et al. (2023). tT paths from *Pecube-D* (this study) are shown in a grey swath that represents a suite of different heat production values (Ao 3.0–4.0 μW/m^3). An asterisk next to the thermochronometric system indicates a mismatch between the *QTQt* and *Pecube* modeled ages for that specific thermochronometric system in that sample.

by 21 Ma to reach a peak temperature of ∼280 °C before 18 Ma (Fig. 4D, E). The eastern end of the roof thrust requires burial at 9–10 km depth at 30 Ma and must remain buried to at least 9 km depth until ∼20 Ma to partially reset ZFT ages.

5.3. Model erosion rate limitations

We evaluated the sensitivity of our modeled erosion rates and resulting thermochronometric ages to 1) out-of-sequence faulting, 2) changes in shortening rates and 3) age of canyon incision. Al-

though our model is able to replicate 84% of the measured ages, notable mismatches include interfluve ZHe ages between 590–620 km, ZHe canyon ages between 600–635 km, and AHe ages in the AP and western EC. Measured ZHe interfluve ages have the largest errors but can still be 5–15 Myr older than modeled, while measured ZHe canyon ages are 4 Myr younger (Fig. 5; Fig. 6, 18PE04, 18PE23). These old interfluve and young canyon ZHe ages overlap in space between 600–620 km.

Two kilometers of OOS fault motion at 635 km did not produce younger ZHe or AFT ages (Fig. S6). While young canyon ZHe ages

can be reproduced with a constant velocity of 3.27 km/Myr, this solution produces canyon ZFT and AFT ages that are too young and cannot replicate any of the interfluve ages (Fig. S7). Varying the age of canyon incision (initiating at 10 Ma or 2.9 Ma) produced no difference in predicted ages.

The large, measured age difference between canyon and interfluve samples may be the result of marked erosion rate variations between canyons and interfluves that were not replicated in our model. We model mean topography from ~50 Ma to ~10 Ma or 2.9 Ma. The modern low-relief plateau edge still exhibits differential relief of 1–2 km, suggesting our modeling approach systematically over-eroded the high elevation interfluves leading to modeled interfluve ZHe ages younger than measured (Fig. 5A). This overpredicted erosion is most discernable in tT-path of sample 18PE04 (Fig. 6). Here, the *Pecube-D* tT-paths are 110–150 °C hotter than the *QTQt* paths between 40–20 Ma, requiring a difference in magnitude (~4–5 km) and time (15 Myr) of exhumation to replicate the cluster of ~34–40 Ma ZHe ages (Fig. 5A).

Our simplified implementation of canyon topography may underpredict erosion rates. The two ZHe canyon dates (18PE23, 18PE28) that are not reproduced by our data are paired with AFT dates that are <2 Ma younger, requiring rapid exhumation at ~8 Ma (635 km) and ~5 Ma (611.2 km) (Figs. 5B, 6J, 6H). This rapid exhumation is reflected in vertical *QTQt* paths at 5 and 3.5 Ma, immediately postdating the measured ages (8 Ma and 5.5 Ma respectively). The more gradual *Pecube-D* generated paths predicted ~12 Ma and 8 Ma ages, missing the measured ages by ~3 Myr. While our model is insensitive to canyon incision since 10 or 2.9 Ma, our simplified implementation of canyon topography precludes pulses of rapid incision that are expected to accompany river incision (Crosby and Whipple, 2006) and may explain these young non-matched ZHe ages.

Comparing tT-paths derived from thermo-kinematic vs. inverse thermal models highlights important changes in deformation or erosional exhumation needed to reproduce measured ages. However, where two different thermal histories (e.g. 18PE61, 18PE26) both replicate measured ages, the differences highlight the non-uniqueness of the tT-paths and suggest a broader range of potential solutions for a given sample (Figs. 5, 6).

5.4. Local vs orogen-scale drivers of exhumation

Newly available thermochronometric ages (Falkowski et al., 2023) and field observations constrain cross-section geometry and kinematics. By comparing the modeled to measured ages, we can start to deconvolve local and orogen-scale drivers of exhumation.

AHe ages as young as 1–2 Ma and AFT ages as young as 2–3 Ma are recorded at the bottom of 2–3 km relief canyons draining the EC across a 250 km distance in southern Peru (Lease and Ehlers, 2013; Gérard et al., 2021; Falkowski et al., 2023). Previous studies have suggested that the young cooling ages in the EC are a result of reactivated faults that act out-of-sequence in response to increased incision (Gérard et al., 2021), or increased incision in the EC driven by Pliocene climate change (Lease and Ehlers, 2013) potentially in the absence of rock uplift or deformation. Our results highlight the importance of canyon incision, but emphasize that the youngest ages across all systems are located immediately east of the active ramp, not in the deepest portion of the canyon (Figs. 3, 5). Canyon incision is required to produce the youngest cooling ages we observe in the EC for all four thermochronometers (Falkowski et al., 2023; Fig. 5). However, the youngest thermochronometers between 600 and 625 km require that incision be accompanied by active ramp uplift and associated regional exhumation for >100 km along strike (e.g. Buford Parks et al., 2023). Structural uplift in the presence of incision affects the modeled ages. Although both ZFT and ZHe ages are reset at higher temperatures and require ex-

humation magnitudes notably larger than the 2–3 km of canyon incision, their modeled ages are sensitive to this incision (Fig. 5). Canyon incision produces modeled ZHe, AFT, and AHe ages that are ~5–12 Myr younger than interfluve ages between 620–650 km and flattens the northeastward trend of increasing model ages that are a function of motion over the basement ramp (Fig. 5). Co-location of active basement ramps and youngest cooling extends over 800 km along the EC into Bolivia (Rak et al., 2017; Buford Parks and McQuarrie, 2019). We propose that incision in the presence of ramp uplift is an orogen-scale driver for the very young cooling ages documented along the plateau edge in southern Peru (Lease and Ehlers, 2013; Gérard et al., 2021; Falkowski et al., 2023).

In the San Gabán canyon ~50 km to the southeast, Buford Parks et al. (2023) showed that the ~10–17 Ma AHe and AFT interfluve ages could not be reproduced with constant shortening rates of 3–4 km/Myr, comparable to the ~3 km/Myr modern SAZ shortening rate in the southern Peruvian Andes (Villegas-Lanza et al., 2016). Buford Parks et al. (2023) argued that a marked decrease in shortening rates from ~4 km/Myr to 0.25–0.6 km/Myr at ~10 Ma was needed to replicate interfluve cooling ages. Our results confirm those of Buford Parks et al. (2023). Our best fit between modeled and measured data is obtained with shortening rates of 3.5 km/Myr that a reduction in shortening rates to ~0.6–1.0 km/Myr from ~10 Ma to Present, emphasizing that a marked slowdown in shortening was a regional tectonic signal in southern Peru. Potential drivers of this slowdown include a decrease in convergence between the Nazca and South American plates between ~9 and ~5 Ma (Espinoza and Iaffaldano, 2023) combined with slab rollback and the associated reduced compressive stress in the overriding plate (Mamani et al., 2010; Holt et al., 2015).

6. Conclusions

A new cross-section through the Eastern Cordillera-Subandean Zone in southern Peru was thermokinematically modeled and able to reproduce observed thermochronometric ages (AHe, AFT, ZHe, AFT). Our model reproduces all the measured canyon AHe, AFT, and ZFT ages and four of seven measured canyon ZHe ages in the Eastern Cordillera and Subandean Zone with a combination of burial, canyon incision, and reduced deformation rate for the final 7 km of shortening. We reproduce the synorogenic basin history in the Altiplano, including the pulses of deformation and sedimentation recorded in the ~40–4 Ma Descanso-Yauri Basin.

Our cross-section exhibits a higher exhumation magnitude than the adjacent San Gabán section (Buford Parks et al., 2023). Reset 14–36 Ma ZFT ages require ~5 km burial below the depth suggested by stratigraphy, which we suggest occurs through the structural repetition of overlying strata and associated basin subsidence. The youngest ZHe (~4 Ma) and ZFT ages (~14 Ma) are a direct result of both the duplexed basement and canyon incision. Doubled basement ramps (Fig. 3) are not present in San Gabán most likely due to pre-existing normal faulting local to that section (Perez et al., 2016).

Similarities between our Marcapata section and the adjacent San Gabán section include the first-order fault geometry, fault kinematics and a marked slowdown in shortening rate suggesting these are orogen-scale features across the southern Peruvian Andes. Young, ~1—4 Ma AHe ages in the San Gabán and our Marcapata section (Lease and Ehlers, 2013; Falkowski et al., 2023) require active uplift over a basement ramp in addition to incision.

CRediT authorship contribution statement

Chloë O. Glover: Data curation, Formal analysis, Investigation, Methodology, Validation, Visualization, Writing – original draft.

Appendix A. Supplementary material

Supplementary material related to this article can be found online at https://doi.org/10.1016/j.epsl.2023.118281.

References

Anderson, R.B., Long, S.P., Horton, B.K., Calle, A.Z., Ramirez, V., 2017. Shortening and structural architecture of the Andean fold-thrust belt of southern Bolivia (21 S): implications for kinematic development and crustal thickening of the central Andes. Geosphere 13 (2), 538–558.

Baby, P., Calderon, Y., Hurtado, C., Bandach, A., 2018a. Atlas of the Peruvian subandean petroleum systems from source to trap. Available at https://www.researchgate.net/publication/334042013_ATLAS_OF_THE_PERU)VIAN_SUBANDEAN_PETROLEUM_SYSTEMS_-_From_source_to_trap.

Baby, P., Calderón, Y., Hurtado, C., Louterbach, M., Espurt, N., Brusset, S., et al., 2018b. The Peruvian sub-Andean foreland basin system: structural overview, geochronologic constraints, and unexplored plays. In: Petroleum Basins and Hydrocarbon Potential of the Andes of Peru and Bolivia AAPG Memoirs. AAPG, pp. 91–121.

Barnes, J.B., Ehlers, T.A., McQuarrie, N., O'Sullivan, P.B., Pelletier, J.D., 2006. Eocene to recent variations in erosion across the central Andean fold-thrust belt, northern Bolivia: implications for plateau evolution. Earth Planet. Sci. Lett. 248 (1–2), 118–133.

Barnes, J.B., Ehlers, T.A., McQuarrie, N., O'Sullivan, P.B., Tawackoli, S., 2008. Thermochronometer record of central Andean Plateau growth, Bolivia (19.5 S). Tectonics 27 (3).

Barnes, J.B., Ehlers, T.A., Insel, N., McQuarrie, N., Poulsen, C.J., 2012. Linking orography, climate, and exhumation across the central Andes. Geology 40 (12), 1135–1138.

Benjamin, M.T., Johnson, N.M., Naeser, C.W., 1987. Recent rapid uplift in the Bolivian Andes: evidence from fission-track dating. Geology 15 (7), 680–683.

Brandon, M.T., Roden-Tice, M.K., Garver, J.I., 1998. Late Cenozoic exhumation of the Cascadia accretionary wedge in the Olympic Mountains, northwest Washington State. Geol. Soc. Am. Bull. 110, 985–1009. https://doi.org/10.1130/0016-7606(1998)110<0985:LCEOTC>2.3.CO;2.

Braun, J., 2003. Pecube: a new finite-element code to solve the 3D heat transport equation including the effects of a time-varying, finite amplitude surface topography. Comput. Geosci. 29, 787–794. https://doi.org/10.1016/S0098-3004(03)00052-9.

Braza, M., McQuarrie, N., 2022. Determining the tempo of exhumation in the eastern Himalaya: Part 1. Geometry, kinematics and predicted cooling ages. Basin Res. 34 (1), 141–169.

Buford Parks, V.M., McQuarrie, N., 2019. Kinematic, flexural, and thermal modelling in the central Andes: unravelling age and signal of deformation, exhumation, and uplift. Tectonophysics 766, 302–325. https://doi.org/10.1016/j.tecto.2019.06.008.

Buford Parks, V.M., McQuarrie, N., Falkowski, S., Perez, N.D., Ehlers, T.A., 2023. Timing and drivers of exhumation and canyon incision in the eastern Peruvian Andes: insights from thermokinematic modelling. Earth Planet. Sci. Lett. https://doi.org/10.1016/j.epsl.2023.118355.

Carlotto, V., Cárdenas, J., 2003. Revisión y actualización del cuadrángulo de Cusco (28-s): Escala 1:50 000. Instituto Geologico y Metalurgico del Peru (INGEMMET).

Cerrón, F., Chacaltana, C., 2003. Memoria descriptiva de la revisión y actualización del cuadrángulo de Ayaviri (30-u), Escala 1:50.000. Instituto Geologico y Metalurgico del Peru (INGEMMET).

Crosby, B.T., Whipple, K.X., 2006. Knickpoint initiation and distribution within fluvial networks: 236 waterfalls in the Waipaoa River, North Island, New Zealand. Geomorphology 82 (1–2), 16–38.

Dahlstrom, C.D.A., 1969. Balanced cross section. Can. J. Earth Sci. 6 (4), 743–757.

Ehlers, T.A., 2005. Crustal thermal processes and thermochronometer interpretation. Rev. Mineral. Geochem. 58, 315–350.

Ehlers, Todd A., 2023. Pecube-D: thermokinematic and erosion modeling software for problems in tectonics and surface processes (1.0 (stable)). Zenodo. https://doi.org/10.5281/zenodo.7785668.

Eichelberger, N., McQuarrie, N., 2015. Three-dimensional (3-D) finite strain at the central Andean orocline and implications for grain-scale shortening in orogens. Bulletin 127 (1–2), 87–112.

Eichelberger, N., McQuarrie, N., Ehlers, T.A., Enkelmann, E., Barnes, J.B., Lease, R.O., 2013. New constraints on the chronology, magnitude, and distribution of deformation within the central Andean orocline. Tectonics 32 (5), 1432–1453. https://doi.org/10.1002/tect.20073.

Eizenhöfer, P.R., McQuarrie, N., Shelef, E., Ehlers, T.A., 2019. Landscape response to lateral advection in convergent orogens over geologic time scales. J. Geophys. Res., Earth Surf. 124, 2056–2078. https://doi.org/10.1029/2019JF005100.

Elger, K., Oncken, O., Glodny, J., 2005. Plateau-style accumulation of deformation: southern Altiplano. Tectonics 24 (4), TC4020.

Espinoza, V., Iaffaldano, G., 2023. Rapid absolute plate motion changes inferred from high-resolution relative spreading reconstructions: a case study focusing on the South America plate and its Atlantic/Pacific neighbors. Earth Planet. Sci. Lett. 604, 118009.

Falkowski, S., Ehlers, T.A., McQuarrie, N., Glover, C.O., Perez, N.D., Buford Parks, V.M., 2023. Exhumation and incision of the eastern Central Andes, southern Peru: low-temperature thermochronology observations. Earth Planet. Sci. Lett. 620. https://doi.org/10.1016/j.epsl.2023.118299.

Farley, K.A., 2000. Helium diffusion from apatite: general behavior as illustrated by Durango fluorapatite. J. Geophys. Res., Solid Earth 105, 2903–2914. https://doi.org/10.1029/1999JB900348.

Gallagher, K., 2012. Transdimensional inverse thermal history modeling for quantitative thermochronology. J. Geophys. Res., Solid Earth 117. https://doi.org/10.1029/2011JB008825.

Garzione, C.N., Auerbach, D.J., Smith, J.J.S., Rosario, J.J., Passey, B.H., Jordan, T.E., Eiler, J.M., 2014. Clumped isotope evidence for diachronous surface cooling of the Altiplano and pulsed surface uplift of the central Andes. Earth Planet. Sci. Lett. 393, 173–181.

Garzione, C.N., Hoke, G.D., Libarkin, J.C., Withers, S., Macfadden, B., Eiler, J., Ghosh, P., Mulch, A., 2017. Rise of the Andes. http://science.sciencemag.org/.

Gautheron, C., Barbarand, J., Ketcham, R.A., Tassan-Got, L., van der Beek, P., Pagel, M., Pinna-Jamme, R., Couffignal, F., Fialin, M., 2013. Chemical influence on α-recoil damage annealing in apatite: implications for (U–Th)/He dating. Chem. Geol. 351, 257–267.

Gérard, B., Robert, X., Audin, L., Valla, P.G., Bernet, M., Gautheron, C., 2021. Differential exhumation of the eastern cordillera in the central Andes: evidence for south-Verging Backthrusting (abancay deflection, Peru). Tectonics 40 (4). https://doi.org/10.1029/2020tc006314.

Ghoshal, S., McQuarrie, N., Robinson, D.M., Adhikari, D.P., Morgan, L.E., Ehlers, T.A., 2020. Constraining central Himalayan (Nepal) fault geometry through integrated thermochronology and thermokinematic modeling. Tectonics 39 (9), e2020TC006156.

Gil, W., 2002. Evolución lateral de la deformación de un frente orogénico: ejemplo de lascuencas subandinas entre 0 y 16 S. Publ. Espec. - Soc. Geol. Perú 4, 146.

Gillis, R.J., Horton, B.K., Grove, M., 2006. Thermochronology, geochronology, and upper crustal structure of the cordillera real: implications for Cenozoic exhumation of the central Andean plateau. Tectonics 25 (6).

Gotberg, N., McQuarrie, N., Caillaux, V.C., 2010. Comparison of crustal thickening budget and shortening estimates in southern Peru (12 14°S): implications for mass balance and rotations in the "Bolivian orocline". Bull. Geol. Soc. Am. 122 (5–6), 727–742. https://doi.org/10.1130/B26477.1.

Holt, A.F., Becker, T.W., Buffett, B.A., 2015. Trench migration and overriding plate stress in dynamic subduction models. Geophys. J. Int. 201 (1), 172–192. https://doi.org/10.1093/gji/ggv011.

Horton, B.K., 2005. Revised deformation history of the central Andes: inferences from Cenozoic foredeep and intermontane basins of the eastern Cordillera, Bolivia. Tectonics 24 (3).

Horton, B.K., 2018. Sedimentary record of Andean mountain building. Earth-Sci. Rev. 178, 279–309.

Horton, B.K., Hampton, B.A., Waanders, G.L., 2001. Paleogene synorogenic sedimentation in the Altiplano Plateau and implications for initial mountain building in the central Andes. Geol. Soc. Am. Bull. 113, 1387–1400.

Horton, B.K., Perez, N.D., Fitch, J.D., Saylor, J.E., 2014. Punctuated shortening and subsidence in the Altiplano Plateau of southern Peru: implications for early Andean mountain building. Lithosphere 7 (2), 117–137. https://doi.org/10.1130/L397.1.

Kar, N., Garzione, C.N., Jaramillo, C., Shanahan, T., Carlotto, V., Pullen, A., Moreno, F., Anderson, V., Moreno, E., Eiler, J., 2016. Rapid regional surface uplift of the northern Altiplano plateau revealed by multiproxy paleoclimate reconstruction. Earth Planet. Sci. Lett. 447, 33–47. https://doi.org/10.1016/j.epsl.2016.04.025.

Ketcham, R.A., Carter, A., Donelick, R.A., Barbarand, J., Hurford, A.J., 2007. Improved modeling of fission-track annealing in apatite. Am. Mineral. 92, 799–810. https://doi.org/10.2138/am.2007.2281.

Kley, J., 1996. Transition from basement-involved to thin-skinned thrusting in the Cordillera Oriental of southern Bolivia. Tectonics 15, 763–775.

Lease, R.O., Ehlers, T.A., 2013. Incision into the eastern Andean plateau during Pliocene cooling. Science 341 (6147), 774–776.

Lease, R.O., Ehlers, T.A., Enkelmann, E., 2016. Large along-strike variations in the onset of subandean exhumation: implications for central Andean orogenic growth. Earth Planet. Sci. Lett. 451, 62–76.

Mamani, M., Worner, G., Sempere, T., 2010. Geochemical variations in igneous rocks of the central Andean orocline (13° S to 18° S): Tracing crustal thickening and magma generation through time and space. Geol. Soc. Am. Bull. 122 (1–2), 162–182.

McQuarrie, N., 2002. The kinematic history of the central Andean fold-thrust belt, Bolivia: implications for building a high plateau. Geol. Soc. Am. Bull. 114 (8), 950–963.

McQuarrie, N., DeCelles, P., 2001. Geometry and structural evolution of the central Andean backthrust belt, Bolivia. Tectonics 20 (5), 669–692. https://doi.org/10.1029/2000TC001232.

McQuarrie, N., Ehlers, T.A., 2015. Influence of thrust belt geometry and shortening rate on thermochronometer cooling ages: insights from thermokinematic and erosion modeling of the Bhutan Himalaya. Tectonics 34 (6), 1055–1079.

McQuarrie, N., Horton, B.K., Zandt, G., Beck, S., DeCelles, P.G., 2005. Lithospheric evolution of the Andean fold–thrust belt, Bolivia, and the origin of the central Andean plateau. Tectonophysics 399 (1–4), 15–37.

McQuarrie, N., Barnes, J.B., Ehlers, T.A., 2008. Geometric, kinematic, and erosional history of the central Andean Plateau. Bolivia (15–17 S). Tectonics 27 (3).

Müller, J.P., Kley, J., Jacobshagen, V., 2002. Structure and Cenozoic kinematics of the eastern Cordillera, southern Bolivia (21 S). Tectonics 21 (5), 1037.

Oncken, O., Hindle, D., Kley, J., Elger, K., Victor, P., Schemmann, K., 2006. Deformation of the central Andean upper plate system—facts, fiction, and constraints for plateau models. In: The Andes. Springer, Berlin, Heidelberg, pp. 3–27.

Perez, N.D., 2015. Cenozoic deformation history of the Andean plateau in southern Peru: Stratigraphic, structural, and geochronologic constraints. University of Texas at Austin. Ph.D. Dissertation.

Perez, N.D., Horton, B.K., 2014. Oligocene-miocene deformational and depositional history of the Andean hinterland basin in the northern Altiplano Plateau, southern Peru. Tectonics 33 (9), 1819–1847. https://doi.org/10.1002/2014TC003647.

Perez, N.D., Levine, K.G., 2020. Diagnosing an ancient shallow-angle subduction event from Cenozoic depositional and deformational records in the central Andes of southern Peru. Earth Planet. Sci. Lett. 541, 116263.

Perez, N.D., Horton, B.K., McQuarrie, N., Stübner, K., Ehlers, T.A., 2016. Andean shortening, inversion and exhumation associated with thin- and thick-skinned deformation in southern Peru. Geol. Mag. 153 (5–6), 1013–1041. https://doi.org/10.1017/S0016756816000121.

Quispesivana Quispe, L.J., Navarro Colque, P.A., 2003. Memoria evisionve de la evisión y actualización de los cuadrángulos de Caravelí (32-p), Chuquibamba (32-q), Chivay (32-s), Cailloma (31-s), Velille (30-s), Livitaca (29-s) y Pacapausa (30-p). Escala 1: 100,000. Instituto Geologico y Metalurgico del Peru (INGEMMET).

Rak, A.J., McQuarrie, N., Ehlers, T.A., 2017. Kinematics, exhumation, and sedimentation of the North central Andes (Bolivia): an integrated thermochronometer and thermokinematic modeling approach. Tectonics 36 (11), 2524–2554.

Reiners, P.W., Spell, T.L., Nicolescu, S., Zanetti, K.A., 2004. Zircon (U-Th)/He thermochronometry: He diffusion and comparisons with 40Ar/39Ar dating. Geochim. Cosmochim. Acta 68, 1857–1887. https://doi.org/10.1016/j.gca.2003.10.021.

Sánchez, A.F., Zapata, A.M. Memoria descriptiva de la revisión y actualización de los cuadrángulos de Sicuani (29-t), Nuñoa (29-u), Macusani (29-v), Limbani (29-x), Sandia (29-y), San Ignacio (29-z), Yauri (30-t), Azángaro (30-v), Putina (30-x), La Rinconada (30-y). Condoroma (31-t), Ocuviri (31-u), Juliaca (31-v), Callalli (32-t), y Ácora (32-x). Escala 1:100 000. Instituto Geologico y Metalurgico del Peru (INGEMMET).

Sánchez Fernández, A.W., Zapata Montes, A.A., 2003a. Memoria evisionve de la evision y actualización de los cuadrángulos de Río Picha (25-p). Timpia (25-q), Chuanquiri (26-p), Quillabamba (26-q), Quebrada Honda (26-r), Parobamba (26-s), Pacaypata (27-p), Machupicchu (27-q), Urubamba (27-r), Calca (27-s), Chontachaca (27-t), Quincemil (27-u), Ocongate (28-t), Corani (28-u) y Ayapata (28-v). Escala 1: 100 000. Instituto Geologico y Metalurgico del Peru (INGEMMET).

Sánchez Izquierdo, J., 2003. Memoria descriptiva de la revisión y actualización de 21 cuadrángulos del llano amazónico Hojas 25-r, 25-s, 25-t, 25-u, 25-v, 25-x, 25-y, 25-z, 26-t, 26-u, 26-v, 26-x, 26-y, 26-z, 27-v, 27-x, 27-y, 27-z, 28-z, 28-y. 28-x.. Escala 1: 100 000. Instituto Geologico y Metalurgico del Peru (INGEMMET).

Saylor, J.E., Horton, B.K., 2014. Nonuniform surface uplift of the Andean plateau revealed by deuterium isotopes in miocene volcanic glass from southern Peru. Earth Planet. Sci. Lett. 387, 120–131. https://doi.org/10.1016/j.epsl.2013.11.015.

Sempere, T., Carlier, G., Soler, P., Fornari, M., Carlotto, V., Jacay, J., Arispe, O., Néraudeau, D., Cárdenas, J., Rosas, S., Jiménez, N., 2002. Late Permian–Middle Jurassic lithospheric thinning in Peru and Bolivia, and its bearing on Andean-age tectonics. Tectonophysics 345 (1–4), 153–181.

Sundell, K.E., Saylor, J.E., Lapen, T.J., Styron, R.H., Villarreal, D.P., Usnayo, P., Cárdenas, J., 2018. Peruvian Altiplano stratigraphy highlights along-strike variability in foreland basin evolution of the Cenozoic central Andes. Tectonics 37 (6), 1876–1904. https://doi.org/10.1029/2017TC004775.

Villegas-Lanza, J.C., Chlieh, M., Cavalié, O., Tavera, H., Baby, P., Chire-Chira, J., Nocquet, J.M., 2016. Active tectonics of Peru: heterogeneous interseismic coupling along the Nazca megathrust, rigid motion of the Peruvian Sliver, and subandean shortening accommodation. J. Geophys. Res., Solid Earth 121 (10), 7371–7394.

Whipp, D.M., Ehlers, T.A., Braun, J., Spath, C.D., 2009. Effects of exhumation kinematics and topographic evolution on detrital thermochronometer data. J. Geophys. Res., Earth Surf. 114, 1–20. https://doi.org/10.1029/2008JF001195.